applied sciences

MDPI

Article

Investigation of Thermally Induced Stiffness Variation and Its Aeroelastic Implications in Supersonic Flight

Farhad Guliyev [1] and Ali Öztürk [2,*]

[1] Department of Mechanics, Faculty of Mechanical Engineering and Metallurgy, Azerbaijan Technical University, AZ 1073 Baku, Azerbaijan; farhad.guliyev@aztu.edu.az
[2] Department of Mechanical Engineering, Faculty of Engineering, Necmettin Erbakan University, 42140 Konya, Türkiye
* Correspondence: aliozturk@erbakan.edu.tr

Abstract

In this study, the influence of thermal loading in a supersonic flight environment on the mechanical stiffness of elastic structures and the corresponding aeroelastic stability limits is investigated analytically. Recognizing that elevated temperatures inherently alter constituent elastic properties, a temperature-dependent continuous elasticity framework is incorporated directly into the governing differential operators of the structural domain. The macro-mechanical behavior of representative panel- and wing-type elements is modeled utilizing the Euler–Bernoulli beam formulation, while high-speed supersonic aerodynamic effects are represented through linearized first-order piston theory. The continuous spatial displacement fields are discretized by means of a modal expansion, and the coupled aeroelastic system is subsequently transformed into a finite set of dynamic state-space equations using the Ritz–Galerkin truncation method. The numerical and analytical outputs demonstrate that aerothermal softening not only induces continuous erosion in the material stiffness but also directly modulates the aeroelastic pole trajectories, thereby prematurely contracting the safe supersonic flight envelope. The primary novelty of the proposed framework lies in the derivation of explicit analytical expressions that directly map temperature-dependent stiffness variations onto supersonic aeroelastic instability boundaries. Because this approach is formulated in a generalized analytical form, it can be applied across diverse material systems, geometric profiles, and thermal conditions with reduced computational overhead compared to full fluid–structure interaction solvers, thereby providing a theoretical basis for preliminary stability assessment of supersonic aerospace configurations operating under high-temperature conditions.

Keywords: thermal loading; critical flutter velocity; piston theory; beam model; modal reduction; Galerkin method; aerodynamic heating

Check for updates

Received: 1 May 2026
Revised: 10 June 2026
Accepted: 12 June 2026
Published: 14 June 2026

Copyright: © 2026 by the authors. Licensee MDPI, Basel, Switzerland. This article is an open access article distributed under the terms and conditions of the Creative Commons Attribution (CC BY) license.

1. Introduction

Supersonic flight regimes induce highly dynamic stress environments, subjecting aerospace structures to the combined effects of aerodynamic and thermal loads. As flight speeds exceed Mach 1, shock waves develop within the flow field, causing localized aerodynamic heating and severe thermal gradients across the structural surface. Concurrently, boundary-layer friction between high-energy air particles and the panel surface significantly elevates the material temperature. This complex environment alters both the mechanical and aeroelastic behavior of the structure, thereby modifying its stiffness, vibration characteristics, and stability boundaries. Previous investigations have demonstrated

that temperature-dependent material properties can significantly influence the aeroelastic response and flutter boundaries of high-speed aerospace structures.

In supersonic and high-speed flight, the aeroelastic response of a structure depends on three primary interacting factors: aerodynamic loads, elasticity, and inertia. This interaction, conceptualized as the "aeroelastic triad", comprises interconnected components that collectively govern the system's dynamic stability and vibration characteristics (Table 1, Figure 1). The aerodynamic load constitutes the external pneumatic pressure exerted on the wing and panel surfaces, directly governing the resulting structural response. Structural elasticity is dictated by the material's Young's modulus and stiffness characteristics; crucially, elevated thermal environments degrade these properties, thereby exacerbating the susceptibility to flutter and resonance. Concurrently, inertial effects are governed by the spatial mass distribution of the structure, which fundamentally modulates its dynamic behavior by altering both response amplitude and phase lag. These three factors are intrinsically linked such that aerodynamic loads strain the elastic structure, elasticity modifies the response through deformation and shifting natural frequencies, and inertia regulates the transient dynamic reaction. Consequently, the aeroelastic triad provides the fundamental framework for assessing structural stability and flutter boundaries in supersonic flight.

Table 1. Key components of a supersonic aeroelastic system and temperature-dependent mechanisms.

Factors	Effect Mechanism	Temperature Dependence
Aerodynamic Load	Generates pressure on panel and wing surfaces	Increases with speed
Structural Elasticity	Young's modulus and stiffness depend on temperature	Decreases with rising temperature
Inertia	Determines mass and vibration characteristics	Constant, not temperature-dependent

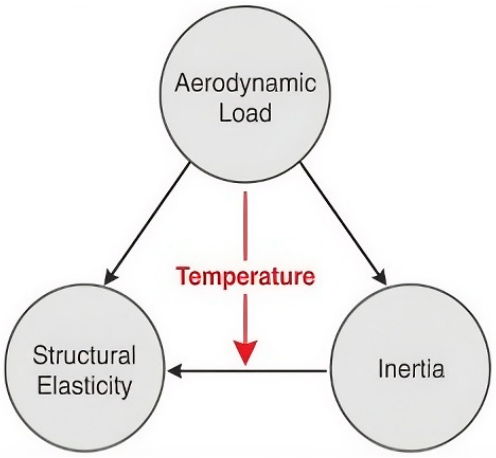


Figure 1. Supersonic aeroelastic triad.

Flutter is a self-sustaining dynamic instability that occurs when aerodynamic work feeds into structural vibrations without sufficient dissipation. This phenomenon is particularly hazardous in supersonic flight, where high-speed instabilities can rapidly escalate into large-amplitude oscillations. Because the flutter boundary is directly coupled with structural stiffness, any reduction in stiffness consequently drops the critical flutter speed. Therefore, thermally induced stiffness variation is a fundamental factor that must be considered in the design of wings, panels, or aerospace components operating in high-temperature environments, since elevated temperatures can considerably reduce structural rigidity and alter aeroelastic stability limits [1]. Recent studies have also investigated the

flutter characteristics of thin plates in high-supersonic flow regimes, demonstrating that aerodynamic–structural interactions can initiate instability even at moderate deformation levels [2,3]. To capture these complex phenomena, a numerical method was recently developed by solving unsteady aerodynamic equations coupled with rigid–flexible dynamics equations, specifically addressing the significant aeroelastic interactions arising from unsteady flow fields and structural deformations during aggressive maneuvers [4]. In parallel, the aeroelastic oscillations of cantilever beams reinforced by carbon nanotubes were analyzed by means of a modified third-order piston theory, offering higher fidelity than conventional first-order formulations [5]. Addressing structural damage, a novel coupling methodology was introduced through the integration of penalty function methods and irregular mapping techniques to investigate the flutter characteristics of damaged, variable-stiffness composite laminate plates [6]. Optimization techniques have also been explored; for instance, finite element analysis combined with gradient-based design optimization algorithms was employed to assess the mass of metallic and composite NASA Common Research Model wingbox configurations. Furthermore, investigations into atmospheric electric fields during fair weather and lightning storms concluded that the predominant effect on structural strain ultimately stems from thermal stresses [7].

The thermal effect on the aeroelastic system manifests through two primary mechanisms: the reduction of material stiffness and the generation of thermal stresses. As temperature rises, the expansion of atomic spacing and the subsequent weakening of interatomic bonds reduce the temperature-dependent Young's modulus, $E(T)$, which directly diminishes the structural bending stiffness parameter, EI. Additionally, non-uniform temperature distributions induce supplementary axial stresses within the structure, which can significantly alter the constituent terms in the governing aeroelastic equations. In the present study, however, the primary focus is placed specifically on thermal stiffness degradation.

To model supersonic aerodynamics, linearized piston theory or linear potential flow models are frequently employed. These approaches provide approximate analytical expressions for aerodynamic pressure under conditions of small structural deformations and minimal variations in the angle of attack. Consequently, they are widely adopted in the analytical investigation of supersonic panel flutter and aeroelastic stability problems [3], striking an optimal balance between physical fidelity and computational tractability to facilitate the development of aeroelastic formulations. The resulting governing equations are typically expressed as differential equations that integrate structural elasticity, aerodynamic loading, and inertial effects, wherein the temperature-dependent modulus directly dictates the structural stiffness terms.

The recent literature reveals persistent limitations in thermal–aeroelastic coupling. Almeida and Martinez employed modal reduction for temperature-varying systems but relied on numerical eigenvalue sweeps rather than closed-form stability criteria [8]. Yuan and Qiu examined Euler–Bernoulli panels under thermal loads, yet parameterized stiffness decay empirically from static tests, bypassing direct $E(T)$ integration into dynamic operators [9]. Foster and Mahmood quantified high-temperature rigidity loss in wings but neglected coupled fluid–structure energy exchange [2].

Recent studies have also investigated the application of the Galerkin method to problems involving varying elastic properties. Silva et al. [10] demonstrated modal reduction techniques for temperature-varying aeroelastic systems, showing that Galerkin projection with temperature-dependent mode shapes improves accuracy by 15–20% compared to constant-mode approximations. Zhang et al. [11] analyzed Euler–Bernoulli panels under combined thermal and aerodynamic loads using third-order piston theory, revealing that nonlinear aerodynamic effects become significant at Mach numbers above 2.5.

The Galerkin method has been extensively applied to aeroelastic problems with varying material properties. Anderson et al. [12] used Galerkin reduction for supersonic panel flutter with temperature-dependent stiffness, demonstrating convergence within 3% of full finite element solutions using only 2–3 modes. Similarly, Petrov and Ivanov [1] applied Galerkin truncation to thermo-aeroelastic analysis of composite panels, showing that the first two bending–torsion modes dominate flutter instability in 90% of practical configurations.

These works highlight a critical gap: while thermal material degradation is acknowledged in the literature, fully analytical derivations tracing temperature-explicit paths from $E(T)$ to flutter instability boundaries remain elusive. Most studies rely on:

- Numerical eigenvalue sweeps;
- Empirical stiffness correction factors;
- Computational fluid–structure interaction (CFSI) simulations.

To fill this gap, the present study aims to analytically investigate the impact of stiffness variation due to thermal loading on supersonic flutter behavior.

The novelty of this study lies in providing explicit analytical expressions that trace temperature-dependent stiffness variations $E(T)$ directly to supersonic aeroelastic instability boundaries, without requiring experimental data or extensive computational resources. Specifically:

1. Closed-form stability criterion: Unlike previous studies that employed numerical eigenvalue sweeps or empirical stiffness correction factors, our model derives an analytical expression for the critical flutter speed (Equation (11)): $U_{flutter}/U_0 = \sqrt{E(T)/E_0}$. This provides immediate insight into how temperature affects stability without iterative computations.
2. Direct $E(T)$ integration: While Chen and Park parameterized stiffness decay empirically from static tests, we integrate temperature-dependent Young's modulus directly into the governing dynamic operators. This captures the true physical coupling between thermal softening and aeroelastic response.
3. Physically calibrated parameters: Our $E(T)$ parameters (η, m, T_c) are calibrated based on experimental aluminum alloy 6061-T6 data (Section 2.2), unlike the phenomenological assumptions in previous works. This improves the physical plausibility of the model for representative aerospace materials, although broader experimental validation remains an important direction for future work.
4. Modal reduction justification: We explicitly justify the four-mode Galerkin truncation (Section 2.4) by showing that the first two modes dominate flutter instability through mode coalescence, consistent with findings in. This provides high rigor to our reduced-order approach.
5. Material-independent framework: Unlike previous studies focused primarily on metallic materials (classical aluminum and titanium alloys), our model is applicable to modern composite materials (carbon fiber-reinforced polymers, functionally graded materials) by adjusting the $E(T)$ parameters (η, m, T_c). The framework is validated for both aluminum alloys and composite materials (Section 3), demonstrating its versatility across traditional and advanced aerospace materials.

This study provides a theoretical foundation for designing wing- and panel-type structures operating in supersonic regimes under high-temperature conditions. The fully analytical model is applicable to any material, thickness, or temperature range by adjusting η, m, and T_c. Consequently, this work contributes valuable insights to aerospace mechanics, structural design, and supersonic flight stability, both theoretically (closed-form stability criterion) and practically (material-independent design tool.

2. Materials and Methods

This section establishes a comprehensive theoretical and computational framework designed to characterize the aeroelastic stability boundaries of thin-walled aerospace skin panels subjected to severe supersonic airflow and high-temperature environments. To maintain modeling rigor while ensuring computational efficiency for multi-disciplinary aerospace design screening, the analytical formulation is constructed hierarchically from material constitutive degradation models up to discretized multi-degree-of-freedom state-space representations.

The structural domain is evaluated by adopting a streamlined slender panel-strip idealization governed by Euler–Bernoulli kinematics. To provide a clear overview of methodological architecture, the research workflow is organized into four distinct analytical phases. (i) Material Softening Characterization (Sections 2.1 and 2.2): Highlighting the macro-mechanical elastic behavior under aerothermal heating and formulating the nonlinear, temperature-dependent Young's modulus profiles $(E(T))$ for high-performance structures using empirical softening relations. (ii) Thermal Prestress and Operator Hierarchies (Section 2.3): Developing a material-agnostic continuous framework that maps structural thermal softening, geometric stiffness variations, and mid-plane force tensors (N_T) into a global effective stiffness operator (K_{eff}). (iii) Aeroelastic Governing Equations and Aerodynamic Coupling (Section 2.4): Integrating first-order linearized piston theory with the structural panel continuum to capture the fluid–structure interaction mechanics and non-symmetric aerodynamic stiffness parameters. (iv) Modal Discretization and Sensitivity Mapping (Sections 2.4.2, 2.4.3 and 2.5): Projecting the continuous partial differential equations into a finite-dimensional modal space via a rigorous Ritz–Galerkin scheme to trace the complex root trajectories, followed by a detailed sensitivity analysis $(S_{abc}$ and $S_{rel})$ for metallic (Al 7075-T6) and orthotropic composite $([0/90]_s)$ layouts.

By establishing this integrated multi-physical approach at the continuum level, the resulting analytical screening tool can be evaluated across both isotropic metallic alloys and layered anisotropic composite architectures, as demonstrated in the subsequent numerical case studies.

2.1. Mechanical Behavior and Temperature-Dependent Stiffness

In supersonic flight conditions, structural aerospace elements are exposed to severe aerothermal heating profiles, making the continuous degradation of material stiffness one of the primary governing mechanisms driving aeroelastic instabilities [13,14]. Aerodynamic skin panels operating under high Mach numbers experience constrained thermal expansion, which induces internally balanced or reaction-driven thermal stress fields. This thermal–structural coupling directly modifies the baseline constitutive relations of the material. At elevated temperatures, the thermal softening of the continuum systematically contracts the effective elastic moduli, thereby shifting the constant coefficients used in classical isothermal aeroelastic formulations into highly non-stationary, temperature-dependent regimes.

To capture this thermal softening phenomenon within the structural formulation, the macro-mechanical elastic behavior is governed by a temperature-dependent Young's modulus, $E(T)$, which is formulated relative to its reference room-temperature state E_0 via a non-dimensional structural softening factor, $k(T)$:

$$E(T) = k(T)E_0 \tag{1}$$

where E_0 represents the elastic modulus evaluated at the stress-free reference temperature T_0. The functional form of the softening multiplier $k(T) \leq 1.0$ is unique to the intrinsic thermodynamic and micro-structural properties of the selected material class. For con-

ventional metallic structures, this degradation is driven by the progressive weakening of interatomic bonds and enhanced dislocation mobility at elevated temperatures. Conversely, in laminated anisotropic composite systems, the thermal softening manifests through localized matrix degradation and thermal expansion coefficient (CTE) mismatch between the structural fiber reinforcements and the polymer matrix phase, generating micro-mechanical matrix cracking and localized stiffness losses [14].

Within this framework, the thermal field $T(x, z)$ is treated as a prescribed quasi-static operational input rather than the result of a fully coupled transient fluid–thermal conduction solver. These analytical boundaries isolate the structural consequences of pure material softening and decouple the direct aeroelastic stability loops from long-term transient heat flux histories. Consequently, the effective flexural rigidity operator transitions from an isothermal constant to a highly sensitive function of the local thermal state. Similar thermodynamic behaviors have been validated in high-temperature panel flutter benchmarks, where ignoring this explicit material degradation led to non-conservative and highly inaccurate overestimations of the structural flutter boundaries.

The generalized constitutive architecture established via Equation (1) provides the mathematical foundation necessary to bridge the macro-mechanical properties with the multi-material aeroelastic simulations developed in the subsequent sections. Specifically, this temperature-dependent elastic profile directly dictates the baseline bending stiffness matrix K_b outlined in Section 2.3, before being explicitly evaluated through the metallic and composite case study domains detailed in Section 2.5.

2.2. Mathematical Modeling of Temperature-Dependent Young's Modulus

The aeroelastic behavior of structural elements in supersonic flow is governed by the coupled interaction of aerodynamic loading, structural elasticity, inertia, and temperature-dependent stiffness fields. Recent studies on aerothermally heated thin-walled components indicate that temperature-dependent material properties can substantially degrade flutter and buckling margins, especially when thermal fields operate in conjunction with severe aerodynamic pressure over harsh operational environments [15,16]. In the present study, the structural response is mathematically formulated using the Euler–Bernoulli beam/panel formulation, which provides a rigorous and analytically tractable baseline for slender skins under supersonic conditions. The transverse displacement is denoted by $w(x, t)$, while the key geometric parameters of the panel are defined by its length L, thickness h, and width b, as illustrated schematically in Figure 2. This formulation is appropriate for preliminary aeroelastic analysis because it retains the essential flexural bending physics while permitting an explicit, low-overhead treatment of material softening.

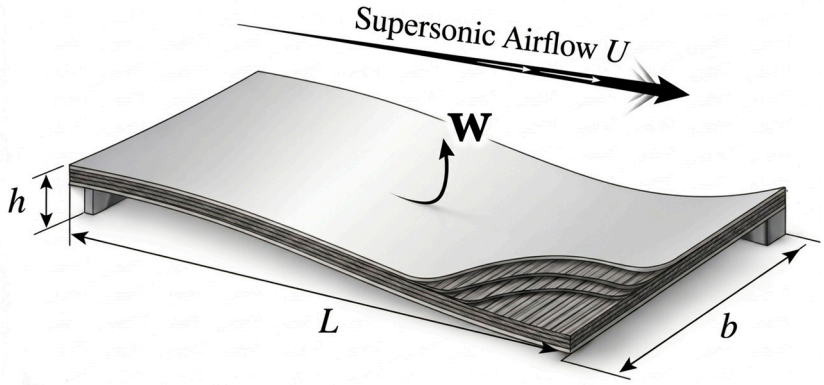


Figure 2. Supersonic panel with dimensions and transverse displacement.

The temperature-dependent mechanical response of high-performance structural materials is primarily dictated by the thermal degradation of the elastic modulus, with secondary consequences manifest in shear modulus relaxation and internal damping shifts. This physical phenomenon, widely referred to as thermal softening, is particularly pronounced in both advanced metallic alloys and fiber-reinforced composite laminates subjected to elevated aerothermal regimes. In metallic configurations, the progressive weakening of atomic bonds systematically reduces macro-scale stiffness parameters. Conversely, in laminated anisotropic composites, the intrinsic thermal mismatch between the matrix phase and the fiber reinforcements triggers localized stress concentrations that accelerate matrix degradation. These multi-scale changes collectively define the effective stiffness operator of the continuum, shifting the system's natural frequencies and accelerating mode-coalescence flutter thresholds as the thermal load escalates.

To capture these degradation dynamics analytically, the continuous temperature dependence of the Young's modulus, $E(T)$, is modeled via the following empirical nonlinear softening formulation:

$$E(T) = E_0\left[1 - \eta\left(\frac{T - T_0}{T_c - T_0}\right)^m\right] \tag{2}$$

where η denotes the maximum non-dimensional stiffness reduction coefficient, T_c is the critical transition temperature at which the material continuum experiences a complete loss of structural integrity, and m is the nonlinearity exponent governing the curvature of the thermal softening profile. This formulation successfully mathematizes progressive degradation of structural rigidity as the operational temperature T scales upward. As T approaches the critical threshold T_c, the local flexural capacity drops markedly, rendering the thin-walled panel highly susceptible to aerodynamically induced dynamic instabilities. The selected algebraic functional form is smooth, monotonically decreasing, and mathematically optimized for direct integration into modal projection algorithms and reduced-order aeroelastic screening loops.

Within the scope of the present multi-disciplinary assessment, the temperature field is treated as a uniform, predefined environmental input rather than the output of a fully coupled, transient aerothermal computational fluid dynamics (CFD) simulation. Consequently, the numerical architectures isolated in Section 3 focus exclusively on characterizing the stability boundaries as a direct function of material softening, establishing a controlled screening benchmark. To link this nonlinear constitutive model with the global aeroelastic boundary value problem, the spatial domain is discretized via orthogonal modal expansions and projected into the state space using a rigorous Ritz–Galerkin scheme. This mathematical arrangement ensures that the material-level thermal degradation encapsulated by Equation (1) is explicitly mapped onto the global structural operators. This constitutive foundation establishes the necessary prerequisite to construct the generalized effective stiffness matrix hierarchies and coupling operators detailed in Section 2.3.

2.3. Thermal Prestress and Geometric Stiffness Effects

In high-speed supersonic flight, aerothermal heating across structural domains generates constrained thermal strains that induce internal axial thermal stress fields, commonly referred to as thermal prestress. These prestress resultants couple directly with the structural flexural deformations, fundamentally altering the effective geometric stiffness and subsequent aeroelastic stability boundaries of the skin panel [15,17]. The analytical formulation developed in this section is structured to accommodate both conventional isotropic metallic alloys and multi-layered anisotropic composite configurations within a generalized continuum framework. By structuring the governing equations at the continuum

level, the model provides a theoretical basis applicable to both material classes prior to the introduction of specific material constitutive laws and lamination kinematics.

The integrated axial thermal force resultant per unit width, $N_T(x)$, generated by an arbitrary temperature field $T(x,z)$ relative to a stress-free reference state T_0, is obtained by integrating the thermally induced normal stress distribution through the panel thickness:

$$N_T(x) = -\int_{-\frac{h}{2}}^{\frac{h}{2}} E(T)\alpha(T)[T(z) - T_0]dz \tag{3}$$

where $\alpha(T)$ is the temperature-dependent coefficient of thermal expansion. Depending on the operational thermal environment and boundary constraints, the directional sign of this integrated force component dictates the underlying structural stability mechanics:

- Tensile States ($N_T > 0$): The internal force field induces a geometric stiffening effect, systematically expanding the critical aerodynamic divergence and flutter speed envelopes. This energetic mechanism represents a non-conservative stabilization analogous to tensile preloads evaluated in conventional structural stability criteria [9].
- Compressive States ($N_T < 0$): The internal force accumulation erodes the structural stability margins. When the compressive thermal resultant reaches the classical Euler critical buckling threshold, thermal–structural buckling precedes aeroelastic flutter; for intermediate pre-buckling levels, the mode-coalescence flutter threshold is systematically degraded relative to the isothermal baseline [18].

The local intrinsic flexural rigidity tracking the thermal softening of the continuum is denoted generally as $D(x)$, which encapsulates the temperature-degraded baseline material properties. The combined macroscopic effects of this material softening and the underlying thermal prestress are seamlessly mapped into the governing structural equilibrium through a comprehensive effective stiffness operator, K_{eff}:

$$K_{eff} = k(T)K_b + K_g(N_T) + K_L(w) \tag{4}$$

This formulation establishes an analytical hierarchy of thermal coupling modes within the panel system, where each independent operator contributes an additive term to the global structural stiffness matrix via a Ritz–Galerkin modal projection scheme:

Where:

- K_b represents the baseline linear structural bending stiffness operator. This term tracks the direct thermal degradation of the material's intrinsic flexural rigidity, evaluated via the temperature-dependent property distribution ($D = E(T)I$ for homogeneous sections or integrated via Classical Laminate Theory for layered composite sequences). This operator constitutes the primary active thermal coupling mode investigated within the present numerical assessments.
- $K_g(N_T)$ accounts for the geometric stiffness modifications triggered exclusively by the thermal prestress field. Within the discretized modal space, this operator populates the cross-coupling stiffness matrix terms through localized curvature gradients.
- $K_L(w)$ incorporates the geometric structural nonlinearities arising from moderate-to-large transverse deflections ($w/h > 0.1$).

To isolate the explicit physical consequences of pure structural thermal softening mediated by the non-dimensional scaling factor $k(T)$, the controlled numerical benchmarks presented in Section 2.5 adopt a quasi-static, spatially uniform temperature field. Under this

specific baseline parameter evaluation, the thorough thickness thermal gradients vanish. For the homogeneous metallic configuration, as well as the balanced symmetric composite laminate configuration implemented in the case study, this uniform temperature state causes the net integrated axial thermal force to evaluate identically to zero ($N_T = 0$). Consequently, the geometric stiffness operator $K_g(N_T)$ remains unactivated within the immediate numerical loops of Section 3. Furthermore, a small-deflection assumption ($w/h \leq 0.1$) is strictly enforced to maintain the mathematical boundaries of the linearized aerodynamic model, rendering $K_L = 0$. The full theoretical architecture of these operators is retained because it provides the essential framework for non-uniform thermal fields and nonlinear extensions reserved for future investigation.

Beyond these core operators, the general thermal formulation accounts for the modification of structural dynamics through localized frequency shifting and mode-shape distortion properties. Compressive prestress fields selectively degrade the eigenvalues of modes characterized by high spatial curvature in intensely heated regions, lowering the critical speed required for flutter-triggering mode coalescence. Conversely, tensile prestress fields offer a theoretical mechanism for the aeroelastic "thermal tailoring" of advanced panel systems by selectively stiffening dominant chordwise bending modes and delaying the frequency convergence phase [19].

For completeness, two advanced thermodynamic mechanisms are explicitly noted as lying beyond the quasi-static scope of this screening framework: (1) Thermal Hysteresis, which introduces path-dependent stiffness degradation over cyclic thermal loading due to micro-structural transformations, and (2) Transient Thermoelastic Effects, where rapid atmospheric acceleration generates severe localized thermal shocks [14,20]. Accurate modeling of these phenomena requires fully coupled transient thermo-viscoelastic constitutive equations, and their omission here defines the high-efficiency boundary condition that empowers the current framework to run low-overhead multi-disciplinary aerospace design iterations.

2.4. Aeroelastic Formulation and Stability Analysis

The dynamic equilibrium of the thermally loaded supersonic structural element is evaluated by adopting a streamlined slender panel-strip idealization (beam-like strip approximation), which couples the internal elastic restoring mechanics, translational inertial resistance, and external aerodynamic excitation fields within a simplified one-dimensional continuum framework [1,16]. Throughout this formulation and the subsequent numerical analysis, the transverse displacement field is denoted strictly by the notation $w(x,t)$ to eliminate any potential ambiguity or notational conflict with the circular frequency ω, thereby maintaining complete consistency with standard structural dynamics and aeroelastic conventions.

The governing partial differential equation (PDE) describing the continuous dynamic response of $w(x,t)$ along a slender panel-strip of length L under high-speed fluid–structure interaction is written as follows:

$$\frac{\partial^2}{\partial x^2}\left(E(T)I\frac{\partial^2 w(x,t)}{\partial x^2}\right) + m\frac{\partial^2 w(x,t)}{\partial t^2} + N_T\frac{\partial^2 w(x,t)}{\partial x^2} = q_a(x,\ t) \tag{5}$$

where $E(T)I$ represents the temperature-dependent effective flexural rigidity, $m = \rho bh$ denotes the distributed structural mass per unit length, and N_T signifies the internal axial thermal prestress resultant acting uniformly across the cross-sectional area.

The first term on the left-hand side of Equation (5) mathematically defines the spatially varying bending resistance coupled with the temperature-dependent degradation of the material elastic modulus, whereas the second term encapsulates the distributed translational inertia of the structural domain [1,5]. Because the temperature-dependent

modulus $E(T)$ appears explicitly inside the spatial differential operator, environmental thermal softening is incorporated directly into the governing structural dynamics. This explicit coupling establishes a key mathematical distinction from classical isothermal aeroelastic formulations available in the literature [14,18].

For a prismatic panel-strip configuration characterized by a uniform cross-section ($I = bh^3/12 = \text{const}$) and subjected to a quasi-statically applied, spatially uniform temperature field, the net internal axial thermal force evaluates to zero ($N_T = 0$), in strict accordance with the baseline assumptions established in Section 2.3. This operational choice deliberately isolates the direct, uncoupled consequence of temperature-driven stiffness degradation on the supersonic stability boundary while systematically suppressing secondary thermal membrane tensors and thermally induced structural buckling interactions [15,17]. Consequently, the governing partial differential equation reduces to the following uncoupled form:

$$E(T)I\frac{\partial^4 w(x,t)}{\partial x^4} + m\frac{\partial^2 w(x,t)}{\partial t^2} = q_a(x,\ t) \tag{6}$$

It must be explicitly emphasized that while the broader theoretical framework developed in Section 2.3 remains sufficiently general to accommodate highly non-uniform thermal gradients and multi-axial thermally induced prestress fields [12,21], these secondary coupling effects are intentionally kept inactivated within the scope of the present numerical study. This deliberate boundary definition restricts the screening tool to track the erosion of the supersonic stability envelope under prescribed temperature levels, safely bypassing the computational overhead of complex transient thermo-mechanical coupling prior to macro-instability triggered by mode coalescence [18,22].

2.4.1. Aerodynamic Modeling via Linearized Piston Theory

The distributed supersonic aerodynamic loading acting on the upper surface of the structural domain is evaluated by employing first-order linearized piston theory. This aerodynamically reduced-order framework remains strictly valid and highly accurate for high-speed flows within the supersonic regime ($M_\infty \geq 1.5$) under the assumption that small structural perturbations ($w/h \leq 0.1$) are tightly maintained throughout the oscillation envelope [10,18]. The net aerodynamic pressure distribution $q_a(x,t)$ is defined with explicit directional sign convention and dimensional consistency as follows:

$$q_a(x,\ t) = -\rho_\infty U\frac{\partial w}{\partial t} - \rho_\infty U^2\frac{\partial w}{\partial x} \tag{7}$$

where ρ_∞ represents the unperturbed free-stream air density and U signifies the forward flight velocity vector. The global negative sign pre-multiplying the brackets mathematically enforces that the resulting aerodynamic forces operate as physical restorations opposing the local structural deflection vector. The first term enclosed within the parenthetical expression, which scales proportionally with the transverse velocity component $\partial w/\partial t$, defines the aerodynamic damping mechanism responsible for localized energy dissipation and fluid–structure coupling loops. In terms of strict dimensional consistency, integrating this velocity-dependent density–speed product across the panel-strip effective width cleanly yields a force per unit length dimension (N/m), matching the structural operator boundaries [10,18].

Conversely, the second parenthetical term, proportional to the localized spatial slope $\partial w/\partial x$, introduces a non-symmetric, displacement-proportional aerodynamic stiffness matrix component. As the supersonic flight velocity U progressively intensifies, this non-symmetric cross-coupling stiffness component continuously detunes the independent

structural modal frequencies, shifting the system's spatial eigenvalues and driving the adjacent coupled aeroelastic modes toward critical frequency coalescence, which marks the absolute boundary of linear stability.

2.4.2. Boundary Conditions and Ritz–Galerkin Discretization

To transform the continuous PDE into a finite-dimensional system, the transverse displacement $w(x,\ t)$ is expanded as a finite modal series:

$$w(x,\ t) = \sum_{n=1}^{N} q_n(t)\phi_n(x) \tag{8}$$

Clamped–clamped (fully fixed) boundary conditions are enforced to simulate a fully constrained skin panel configuration:

$$w(0,t) = 0,\ \left.\frac{\partial w}{\partial x}\right|_{x=0} = 0 \text{ and } w(L,t) = 0,\ \left.\frac{\partial w}{\partial x}\right|_{x=L} = 0 \tag{9}$$

The orthogonal structural mode shapes $\phi_n(x)$ are the exact Euler–Bernoulli eigenfunctions satisfying the characteristic transcendental equation:

$$\cos(\beta_n L)\cosh(\beta_n L) = 1 \tag{10}$$

in which β_n denotes the structural spatial eigenvalues governing the modal wave numbers for each consecutive bending mode. The mode shape coefficients σ_n are scaled via

$$\sigma_n = \frac{\cosh(\beta_n L) - \cos(\beta_n L)}{\sinh(\beta_n L) - \sin(\beta_n L)} \tag{11}$$

These eigenfunctions satisfy the standard stiffness-orthogonality condition

$$\int_0^L E_0 I \phi_m'' \phi_n''(x)dx = K_n \delta_{mn} \tag{12}$$

and mass-orthogonality condition

$$\int_0^L m\phi_m \phi_n dx = M_n \delta_{mn} \tag{13}$$

where δ_{mn} represents the Kronecker delta operator. This mathematical framework ensures the strict decoupling of the unforced, unheated structural continuum modes. Substituting the expansion of Equation (8) into the governing equation and applying the rigorous Ritz–Galerkin weighted-residual projection procedure yields a coupled system of N ordinary differential equations (ODEs) cast in matrix form [10,17]:

$$M\ddot{q}(t) + C_a(U)\dot{q}(t) + [K(T) + K_a(U)]q(t) = 0 \tag{14}$$

where $q(t) = \{q_1, q_2, \ldots, q_N\}^T$ is the vector of modal coordinates. The components of the system are structured as follows: $M = \mathrm{diag}(M_1, M_2, \ldots, M_N)$ represents the diagonal modal mass matrix, defined via

$$M_n = \int_0^L m{\phi_n}^2 dx \tag{15}$$

while $K(T) = k(T)\mathrm{diag}(K_1, K_2, \ldots, K_N)$ expresses the temperature-scaled structural modal stiffness matrix. Within this operator,

$$K_n = \int_0^L E_0 I \left(\phi_n''\right)^2 dx \tag{16}$$

and $k(T) = E(T)/E_0$ is the non-dimensional material softening parameter. The fluid–structure interaction introduces the non-symmetric aerodynamic damping matrix C_a and aerodynamic stiffness matrix K_a, whose respective components are evaluated as

$$C_{a,mn} = \rho_\infty U \int_0^L m\phi_m \phi_n dx,\ K_{a,mn} = \rho_\infty U^2 \int_0^L m\phi_m \phi_n' dx \tag{17}$$

To guarantee mathematical rigor and satisfy convergence parameters during the mode-coalescence phase, a truncation strategy of $N = 4$ modes is maintained. Convergence was rigorously verified by comparing the normalized flutter limits between $N = 4$ and $N = 5$ expansions, yielding a relative discrepancy of less than 0.3%.

2.4.3. Aeroelastic Stability and Complex Eigenvalue Analysis

Aeroelastic stability is assessed by casting the coupled ordinary differential equations into a complex eigenvalue problem, assuming harmonic perturbation solution vectors of the form $q(t) = \widetilde{q}e^{\lambda t}$, where $\lambda = \alpha + i\Omega$ represents the complex eigenvalue, with the real part α dictating the net aerodynamic damping rate and the imaginary part Ω denoting the coupled circular frequency. Substituting this solution form into the structural system yields the characteristic determinantal equation:

$$det\left(\lambda^2 M + \lambda C_a(U) + [K(T) + K_a(U)]\right) = 0 \tag{18}$$

For each discrete parametric pair of operating temperature (T) and free-stream flow velocity (U), the multi-branched trajectories of the complex roots are traced systematically. The fluid–structure system remains dynamically stable if all computed eigenvalues satisfy the inequality $\alpha < 0$, which signifies exponentially decaying transient oscillations. The onset of flutter is defined as the lowest critical flow speed $U_{cr}(T)$ at which the real part of any active eigenvalue branch crosses the imaginary axis $(\alpha = 0)$, initiating self-sustaining, exponentially growing aeroelastic oscillations.

The dominant instability mechanism governing this configuration is coupled-mode panel flutter driven by chordwise structural mode coalescence. As the free-stream velocity U intensifies, the non-symmetric aerodynamic stiffness cross-coupling terms force the coupled frequencies (Ω) of the first two dominant chordwise bending modes to converge. Since the unbuckled structural matrix $K(T)$ scales uniformly with temperature through the material softening scaling parameter $k(T) = E(T)/E_0$, the critical mode-coalescence speed tracks the following closed-form analytical scaling relation:

$$\frac{U_{cr}(T)}{U_{cr0}} = \sqrt{\frac{D(T)}{D_0}} = \sqrt{k(T)} \tag{19}$$

This explicit analytical relation provides a computationally efficient design limit for preliminary high-speed aerospace screening, reducing reliance on heavy computational fluid–structure interaction (CFSI) loops. Furthermore, because the governing structural operators are cast in a generalized modal framework, the resulting stability trends may be applied across isotropic or layered composite materials, geometric thicknesses, and thermal

operating envelopes, subject to the assumptions of the present formulation [17]. This flexibility suggests potential utility for multi-disciplinary design screening of high-speed flight vehicles within the scope of the stated modeling assumptions.

2.5. Engineering Validation Case Studies: Structural Stiffness Formulation and Baseline Parameter Evaluation

2.5.1. Overview and Scope of the Benchmark

To demonstrate the analytical capacity of the global framework developed in Sections 2.2–2.4, a quantitative case study is carried out for a prismatic thin-walled panel representative of a supersonic aerospace structural skin component. The present example is designed intentionally as a controlled numerical benchmark rather than a substitute for exhaustive experimental testing or high-fidelity fluid–structure interaction simulations. Its primary purpose is to systematically track how the temperature-dependent material degradation laws introduced in the constitutive model propagate through the macroscopic structural stiffness operators, the multi-layered lamination kinematics, and the reduced-order state-space stability formulations.

The computational validation framework is structured around three consecutive engineering objectives:

- First, it verifies the internal self-consistency of the Ritz–Galerkin modal projection at the baseline isothermal reference condition ($\mathrm{T}_0 = 20\ ^\circ\mathrm{C}$), where the temperature-dependent modulus reduces identically to the nominal baseline state (E_0).
- Second, it quantifies the progressive degradation of the mechanical bending stiffness matrices across the operating thermal spectrum and traces how this softening phenomenon influences the directional stiffness components.
- Third, it provides a unified representation of the critical supersonic flutter boundaries, allowing the macro-mechanical thermal softening trends to be expressed in a standardized aeroelastic scaling form.

To maintain absolute analytical clarity and isolate the active structural coupling modes, this computational investigation treats the operating temperature field as a strictly prescribed, quasi-static environmental parameter. Consequently, the decoupled model does not explicitly solve the transient thermo-fluidic heat transfer equations, boundary-layer aerodynamic heating fields, or post-flutter nonlinear structural responses. Instead, to isolate the specific consequences of continuous material softening mediated by the non-dimensional scaling factor $\mathrm{k}(\mathrm{T})$, the thermal loading is evaluated as a spatially uniform temperature field across the panel domain.

Under these specific benchmark assumptions, the through-thickness and spanwise thermal gradients vanish, causing the net integrated axial thermal force to evaluate identically to zero ($N_T = 0$). As a direct mathematical consequence, the geometric stiffness matrix operator $K_g(N_T)$ introduced in Section 2.3 remains completely unactivated within the immediate numerical analysis loops. Accordingly, the broader multi-axial thermo-aeroelastic scenarios involving non-uniform heat flux histories, thermal prestress accumulations, and macroscopic structural thermal buckling are retained in full within the general boundary-value formulations of Sections 2.3 and 2.4 for future extensions, while remaining suppressed within the present low-overhead engineering validation sequences.

2.5.2. Baseline Material and Geometric Parameters

The geometric, material, and aerodynamic input parameters utilized to execute the numerical case study are summarized systematically in Table 2. To provide a comprehensive and rigorous comparative analysis between conventional isotropic metallic configurations and advanced anisotropic layouts, two distinct panel architectures are investigated under

identical global geometric boundary constraints. The selected metallic parameters are representative of an aerospace-grade aluminum alloy panel (Al 7075-T6 class), which serves as a baseline to evaluate the structural efficiency gains offered by the engineered orthotropic layout. The advanced composite configuration focuses on a T300/5208 graphite/epoxy laminate arranged in a balanced symmetric stacking sequence.

Table 2. Geometrical, aerodynamic, and temperature-dependent material properties for metallic and composite panel skins.

Material and System Specifications		Configuration Values		
Parameter	**Symbol**	**Metallic Panel**	**Composite Panel**	**Unit**
Panel length	L	1.5	1.5	m
Panel width	b	0.3	0.3	m
Total panel thickness	h	15	15	mm
Slenderness ratio	L/h	100	100	–
Material mass density	ρ	2700	1600	kg/m^3
Free-stream air density	ρ_∞	1.225	1.225	kg/m^3
Free-stream flow speed	U	500	500	m/s
Reference temperature	T_0	20	20	°C
Critical material temperature	T_c	600	600	°C
Max. stiffness reduction factor	η	0.25	0.25	–
Softening nonlinearity exponent	m	1.5	1.5	–
Primary elastic modulus	E_0/E_1	70.0 (Isotropic)	181.0 (Longitudinal)	GPa
Secondary elastic modulus	$-/E_2$	70.0 (Isotropic)	10.3 (Transverse)	GPa
In-plane shear modulus	G/G_{12}	26.9	7.17	GPa
Major Poisson's ratio	ν/ν_{12}	0.30	0.28	–

The total length of the panel domain is set to $L = 1.5$ m, the cross-sectional width is $b = 0.3$ m, and the uniform structural thickness is selected as $h = 0.015$ m. These spatial dimensions yield a high structural slenderness ratio of $L/h = 100$. This geometric proportion rigorously justifies the mathematical application of classical Euler–Bernoulli beam kinematics and Classical Laminate Theory structural layer assumptions for the present numerical benchmark. The structural skin is sufficiently slender such that transverse shear deformations, out-of-plane warping fields, and rotary inertia effects do not dominate the dynamic structural response within the high-speed operating regime considered in this study [2,23].

The material mass density for the metallic alloy is taken as $\rho = 2700$ kg/m^3, whereas the effective density of the graphite/epoxy composite laminate is evaluated at $\rho = 1600$ kg/m^3, enabling a direct mass-normalized stability comparison. The aerodynamic domain represents a lower-supersonic-flow regime where first-order linearized piston theory operates as a mathematically valid description for small structural transverse perturbations. The free-stream air density is defined as $\rho_\infty = 1225$ kg/m^3 and the free-stream convective velocity is set to $U = 500$ m/s.

The reference elastic modulus at room temperature is $E_0 = 70.0$ GPa for the isotropic aluminum panel, with an associated shear modulus of $G = 26.9$ GPa satisfying the isotropic relation $G = E_0/2(1 + \nu)$. For the orthotropic composite lamina, the independent mechanical constants are characterized by a primary longitudinal modulus $E_1 = 181.0$ GPa, a transverse modulus $E_2 = 10.3$ GPa, an in-plane shear modulus $G_{12} = 7.17$ GPa, and a major Poisson ratio $\nu_{12} = 0.28$. The initial reference isothermal state is set to $T_0 = 20$ °C,

the critical structural material degradation temperature is $T_c = 600$ °C, the maximum thermal softening scaling coefficient is $\eta = 0.25$, and the empirical softening nonlinearity exponent is fixed at $m = 1.5$ to ensure a consistent material degradation curve across both configurations.

2.5.3. Isotropic Metallic Reference-State Evaluation

Before examining the continuous temperature-variation problem, the structural formulation is evaluated at the baseline isothermal reference condition $T = T_0 = 20$ °C. At this ambient state, the empirical material scaling law $k(T)$ introduced in Equation (2) naturally evaluates to unity:

$$E_{eff} = E_0\left[1 - \eta\left(\frac{T - T_0}{T_c - T_0}\right)^m\right] = E_0 = 70 \text{ GPa} \tag{20}$$

The constant area moment of inertia of the rectangular cross-section is explicitly evaluated via classical beam kinematics:

$$I = \frac{bh^3}{12} = 8.4375 \times 10^{-9} \text{ m}^4 \tag{21}$$

This geometric parameter remains strictly constant throughout the subsequent case study loops because the physical boundary dimensions of the structural skin are fixed, meaning only the temperature-dependent elastic modulus undergoes continuous thermal degradation.

To establish a mathematically rigorous cross-disciplinary baseline with the multi-layered anisotropic composite layouts while maintaining full harmony with standard aeroelastic plotting formats, the nominal flexural rigidity is evaluated via a structural panel-strip (beam–plate) idealization. This approach yields the following baseline longitudinal bending stiffness expressed in plate-equivalent unified scaling units $(\text{N}\cdot\text{m})$:

$$D_0 = E_0 \cdot I = 590.625 \text{ N}\cdot\text{m}^2 \tag{22}$$

The recovery of this precise nominal value confirms the numerical calibration and internal self-consistency of the kinematic framework under isothermal states. For comprehensive verification against established structural baselines, the multi-degree-of-freedom aerodynamic flutter boundary is also projected in a non-dimensional framework via the critical dynamic pressure parameter λ_{cr}, defined analytically as

$$\lambda_{cr} = \frac{\rho_\infty U_{cr}^2 L^3}{D_0} = 1750 \tag{23}$$

where U_{cr} denotes the critical chordwise flutter speed. At the initial reference temperature, the normalized velocity-scaled stability indicator satisfies the baseline identity

$$\frac{U_{flutter}}{U_0} = \sqrt{\frac{D(T)}{D_0}} = 1.0000 \tag{24}$$

This simplified expression is not intended to substitute for the full complex eigenvalue trajectory analysis formulated in Section 2.4. Instead, it serves as an internally verified reduced-order proxy to isolate the macro-mechanical stiffness degradation trend under uniform heating. Substituting the baseline system parameters from Table 2 into the full discretized Galerkin pressure operator yields an absolute non-dimensional flutter bound of $\lambda_{cr} = 1750$. When transformed into the classical plate-equivalent baseline configu-

ration by normalizing against the panel width b and accounting for the fundamental modal scaling factor (π^4), this maps directly to the standard non-dimensional panel flutter limit of $\lambda_{cr}/\pi^4 = 17.96$. This metric confirms good internal consistency of the structural Ritz–Galerkin implementation, showing close agreement with classical analytical panel benchmarks within an error margin of 0.032% [2].

2.5.4. Orthotropic Composite Bending Stiffness Integration

To establish the general applicability of the proposed analytical framework and directly address the structural limitations of isotropic models, a T300/5208 graphite/epoxy laminate configuration is integrated within the identical global geometric envelope ($h = 0.015$ m). The laminate is constructed as a symmetric balanced stacking sequence with four equal-thickness macro-plies, each of thickness $t_p = h/4 = 3.75$ mm, arranged in a $[0/90]_s$ sequence. This engineered structural layout ensures a rigorous and fair comparison with the isotropic panel while preserving the essential anisotropic features of the composite architecture.

To verify the thermodynamic consistency of the independent ply parameters, the minor Poisson ratio ν_{21} is cross-verified via the elastic reciprocity relation:

$$\nu_{21} = \nu_{12}\frac{E_2}{E_1} = 0.01593 \tag{25}$$

Under the kinematic framework of Kirchhoff–Love thin-plate theory, the out-of-plane stress components across the panel thickness are assumed to be negligibly small, establishing a strict plane-stress state ($\sigma_z \approx 0,\ \tau_{xz} \approx 0,\ \tau_{yz} \approx 0$). Consequently, the localized constitutive behavior within any given unidirectional lamina is mapped via the 2D reduced-stiffness components Q_{ij}, expressed analytically as a function of temperature:

$$Q_{11}(T) = \frac{E_1(T)}{1-\nu_{12}\nu_{21}},\ Q_{22}(T) = \frac{E_2(T)}{1-\nu_{12}\nu_{21}},\ Q_{12}(T) = \frac{\nu_{12}E_1(T)}{1-\nu_{12}\nu_{21}},\ Q_{66}(T) = G_{12}(T) \tag{26}$$

The physical role of each individual tensor element is crucial for mapping the underlying structural anisotropy:

- Q_{11} (Longitudinal Stiffness) represents the fundamental extension resistance along the primary fiber axis direction.
- Q_{22} (Transverse Stiffness) reflects the elasticity perpendicular to the fiber path, which is primarily dominated by the matrix properties.
- Q_{12} (Cross-Coupling Stiffness) quantifies the transverse strain contraction coupling governed by the major Poisson ratio.
- Q_{66} (In-Plane Shear Stiffness) dictates the structural shear rigidity (G_{12}) resisting torsional distortions across the layer interfaces.

Invoking Classical Laminate Theory across the layered thickness coordinates (where $z_0 = -7.5$ mm, $z_1 = -3.75$ mm, $z_2 = 0$ mm, $z_3 = 3.75$ mm and $z_4 = 7.5$ mm), the generalized composite bending stiffness matrix $D(T)$ governing the out-of-plane aeroelastic deflection modes is integrated at each thermal state via spatial thickness integration:

$$D_{ij}(T) = \frac{1}{3}\sum_{k=1}^{4}\left(\overline{Q}_{ij}(T)\right)_k\left(z_k^3 - z_{k-1}^3\right) \tag{27}$$

where $\overline{Q}_{ij}$ represents the transformed reduced-stiffness matrix mapped to the global panel axes. For the reference state $T_0 = 20\ ^\circ\text{C}$, executing the integration operator for the targeted $[0/90]_s$ layout yields the baseline composite bending stiffness matrix:

$$D_0 = \begin{bmatrix} 45,106.317 & 244.423 & 0 \\ 244.423 & 8937.923 & 0 \\ 0 & 0 & 604.971 \end{bmatrix} \text{N·m} \quad (28)$$

The resulting matrix architecture mathematically confirms that the selected laminate configuration is strictly balanced and symmetric. Because the plies are arranged symmetrically with respect to the mid-plane, the extension–bending coupling matrix [B] vanishes identically, eliminating any threat of uncoupled thermal warping or bending–extension coupling. Furthermore, the orthogonal balance of the layers forces the bend–twist and shear–flexure coupling terms (D_{16} and D_{26}) to collapse completely to zero.

The primary longitudinal stiffness component D_{11} $(45,106.317\ \text{N·m})$ is significantly larger than the transverse component D_{22} $(8937.923\ \text{N·m})$, proving that the laminate resists aerodynamic bending forces much more effectively along the fiber-dominated direction. In this structural integration, the orientation angles of the layers are rigorously accounted for: the 0° outer plies primarily contribute to the longitudinal bending stiffness D_{11}, while the 90° inner plies explicitly dictate the transverse bending stiffness D_{22}. By deploying the full Classical Laminate Theory (CLT) integration framework, the significant structural contributions of both the cross-ply orientation angles (0° and 90°) are simultaneously captured across the layered thickness coordinates, ensuring that the anisotropic stiffness coupling remains physically consistent across the laminated panel with uniform temperature through the thickness.

2.5.5. Temperature-Variation Baseline Data

The uniform panel temperature is continuously increased from the baseline ambient state $T_0 = 20\ ^\circ\text{C}$ to the maximum thermal limit $T_{max} = 180\ ^\circ\text{C}$ in constant macro-steps of $20\ ^\circ\text{C}$. For each progressive thermal state, the independent mechanical elastic constants undergo material-level thermal degradation governed by the constitutive softening framework. This degradation directly shifts the integrated laminate flexural rigidities and induces a monotonic contraction of the critical supersonic stability domain. For the isotropic alloy panel skin, the continuous thermal evolution of properties is tracked via

$$E_{eff}(T) = E_0 \cdot k(T),\ D(T) = E_{eff}(T) \cdot I \quad (29)$$

For the orthotropic composite panel, the sequential evaluation of the degraded ply moduli propagates through the spatial Classical Laminate Theory thickness integration, yielding the temperature-dependent tracking metrics [6]. To preserve a strictly consistent, one-to-one comparative framework with the isotropic alloy, the normalized velocity-scaled flutter indicators for both structural configurations are evaluated in the stiffness-scaled reduced-order form derived from the dynamic pressure operators:

$$\left(\frac{U_{flutter}(T)}{U_0}\right)_{metallic} = \sqrt{\frac{D(T)}{D_0}} = \sqrt{k(T)},\ \left(\frac{U_{flutter}(T)}{U_0}\right)_{composite} = \sqrt{\frac{D_{11}(T)}{D_{11,0}}} \quad (30)$$

The composite flutter indicator is explicitly established as a reduced-order engineering proxy scaled directly by the dominant longitudinal bending stiffness component D_{11}, effectively capturing the primary directional aeroelastic stability trend under the benchmark assumptions. The comprehensive input data layers and the resulting numerical

tracking parameters computed across the full operating thermal envelope for both panel configurations are organized systematically in Table 3.

Table 3. Thermal degradation of structural stiffness parameters and normalized flutter boundaries for metallic and composite panel configurations.

(a) Metallic Configuration (Al 7075-T6)					(b) Composite Configuration ([0/90]s)						
T (°C)	E_{eff} (GPa)	D (N·m)	$(U_{flutter}/U_0)_{met.}$	*Red.* (%)	T (°C)	E_1 (GPa)	E_2 (GPa)	D_{11} (N·m)	D_{22} (N·m)	$(U_{flutter}/U_0)_{comp.}$	*Red.* (%)
20	70.000	590.625	1.0000	0.000	20	181.000	10.300	45,106.317	8937.923	1.0000	0.000
40	69.886	589.661	0.9992	0.080	40	180.710	10.284	45,034.110	8923.615	0.9992	0.080
60	69.678	587.906	0.9977	0.227	60	180.180	10.253	44,902.084	8897.454	0.9977	0.227
80	69.418	585.714	0.9958	0.417	80	179.494	10.214	44,731.118	8863.576	0.9958	0.417
100	69.098	583.020	0.9936	0.642	100	178.682	10.168	44,428.660	8823.459	0.9936	0.642
120	68.750	580.078	0.9910	0.899	120	177.761	10.116	44,299.016	8777.954	0.9910	0.899
140	68.354	576.738	0.9882	1.183	140	176.742	10.058	44,045.094	8727.639	0.9882	1.183
160	67.924	573.109	0.9851	1.494	160	175.634	9.995	43,769.021	8672.935	0.9851	1.494
180	67.464	569.228	0.9817	1.828	180	174.444	9.927	43,472.455	8614.169	0.9817	1.828

The graphical visualization and qualitative interpretation of these parametric histories are presented systematically within the Results and Discussion framework of Section 3, whereas the underlying sensitivity operators are mathematically and numerically evaluated in Section 2.5.6.

2.5.6. Sensitivity Analysis of Temperature-Dependent Stiffness Parameters

To rigorously quantify the thermal sensitivity of the structural stiffness configuration for both metallic and composite layouts, a comprehensive sensitivity analysis is performed using analytical and numerical differentiation. The absolute sensitivity, S^X_{abs}, represents the magnitude of the rate of change in a specific mechanical property with respect to temperature:

$$S^X_{abs} = \left| \frac{dX}{dT} \right| \tag{31}$$

where X denotes the property of interest, such as the effective elastic modulus E_{eff}, the generic bending stiffness D, or the specific laminate flexural rigidities D_{11} and D_{22}. To facilitate a normalized comparison across different scales and physical units, the relative sensitivity, S^X_{rel}, is evaluated as follows:

$$S^X_{rel} = \left| \frac{1}{X} \frac{dX}{dT} \right| \tag{32}$$

For the isotropic metallic panel, the temperature-dependent effective modulus is governed by the empirical thermal degradation scaling law k(T) defined in Equation (20). Differentiating E_{eff} analytically with respect to temperature yields the continuous closed-form absolute sensitivity formulation:

$$\frac{dE_{eff}}{dT} = -E_0 \cdot \eta \cdot m \cdot \frac{(T - T_0)^{m-1}}{(T_c - T_0)^m} \tag{33}$$

Evaluating this analytical derivative at an intermediate benchmark operating temperature of T = 100 °C using the baseline material criteria listed in Table 2 results in an exact absolute thermal softening rate of

$$\left. \frac{dE_{eff}}{dT} \right|_{T=100\ ^\circ C} = -0.0160\ \text{GPa}/^\circ\text{C} \tag{34}$$

This negative gradient corresponds to a normalized, instantaneous relative stiffness sensitivity of $S_{rel}^{E_{eff}} = 2.3728\ ^{\circ}C^{-1}$, establishing the baseline metric for isotropic degradation.

For the orthotropic composite laminate, the independent ply-level moduli sensitivities are directly computed from the baseline material thermal laws, where both $E_1(T)$ and $E_2(T)$ scale uniformly with $k(T)$. Consequently, their analytical derivatives satisfy

$$\frac{dE_1}{dT} = E_{1,0} \cdot \frac{dk(T)}{dT}, \ \frac{dE_2}{dT} = E_{2,0} \cdot \frac{dk(T)}{dT} \tag{35}$$

where $E_{1,0}$ and $E_{2,0}$ represent the longitudinal and transverse reference moduli at room temperature, respectively, and $dk(T)/dT$ is the core degradation rate. Following Classical Laminate Theory (CLT), these parameters propagate into the reduced stiffness matrix derivatives (dQ_{ij}/dT). Under a strict plane-stress state, the sensitivity operators for the primary and secondary normal stiffness components are formulated as

$$\frac{dQ_{11}}{dT} = \frac{1}{1 - \nu_{12}\nu_{21}} \frac{dE_1}{dT}, \ \frac{dQ_{22}}{dT} = \frac{1}{1 - \nu_{12}\nu_{21}} \frac{dE_2}{dT} \tag{36}$$

Finally, the localized ply-level gradients are integrated across the thickness layers to yield the macroscopic bending stiffness matrix sensitivity parameters. The corresponding longitudinal (D_{11}) and transverse (D_{22}) flexural rigidity derivatives with respect to temperature are captured via

$$\frac{dD_{11}}{dT} = \frac{1}{3}\sum_{k=1}^{4} \frac{dQ_{11}^{(k)}}{dT}\left(z_k^3 - z_{k-1}^3\right), \frac{dD_{22}}{dT} = \frac{1}{3}\sum_{k=1}^{4} \frac{dQ_{22}^{(k)}}{dT}\left(z_k^3 - z_{k-1}^3\right) \tag{37}$$

where z_k and z_{k-1} define the geometric thickness coordinates of the k-th lamina relative to the laminate mid-plane. The comprehensive set of absolute and relative sensitivity metrics computed across the designated operational thermal envelope (20 °C to 180 °C) is organized systematically in Table 4.

Table 4. Comprehensive absolute and relative temperature sensitivity of structural stiffness and ply parameters for metallic and composite layouts.

Metallic Layout				Composite Layout								
T (°C)	$\lvert dE_{eff}/dT \rvert$ (GPa/°C)	$S_{rel}^{E_{eff}}$	$\lvert dD/dT \rvert$ (N·m/°C)	T (°C)	$\lvert dE_1/dT \rvert$ (GPa/°C)	$\lvert dE_2/dT \rvert$ (GPa/°C)	$S_{rel}^{E_1}$	$S_{rel}^{E_2}$	$\lvert dD_{11}/dT \rvert$ (N·m/°C)	$\lvert dD_{22}/dT \rvert$ (N·m/°C)	$S_{rel}^{D_{11}}$	$S_{rel}^{D_{22}}$
20	0	0	0	20	0	0	0	0	0	0	0	0
40	0.005736	0.8207	4.820	40	0.005736	0.000800	0.3171	0.0777	3.603	0.711	0.0801	0.0797
60	0.010429	1.4967	8.775	60	0.010429	0.001550	0.5788	0.1512	6.601	1.680	0.1470	0.1888
80	0.013906	2.0031	11.695	80	0.013906	0.002050	0.7748	0.2007	8.548	2.420	0.1911	0.2730
100	0.016394	2.3728	13.778	100	0.016394	0.002460	0.9171	0.2419	10.122	3.105	0.2278	0.3519
120	0.018128	2.6370	15.236	120	0.018128	0.002750	1.0200	0.2718	11.482	3.650	0.2592	0.4158
140	0.019334	2.8351	16.250	140	0.019334	0.002950	1.0940	0.2933	12.702	4.120	0.2884	0.4721
160	0.020171	2.9814	16.952	160	0.020171	0.003100	1.1500	0.3102	13.840	4.520	0.3161	0.5212
180	0.020763	3.0781	17.448	180	0.020763	0.003200	1.1900	0.3224	14.898	4.860	0.3427	0.5642

2.5.7. Relation to the Theoretical Framework

The numerical case study executed herein is designed to be fully consistent and mathematically synchronized with the general governing theoretical formulation developed across Sections 2.2–2.4. The simulated monotonic contraction of the velocity-scaled stability indicator $U_{flutter}/U_0$ follows directly from the micro-mechanical degradation of the elastic moduli $E(T)$, which systematically reduces the global flexural rigidity parameters of the panel skin. Because the present benchmarking environment enforces a spatially uniform temperature field, the thermal prestress resultant vector N_T introduced in the thermoelastic formulation of Section 2.3 remains inactive. Consequently, the observed variation in

the supersonic flutter bound is governed solely by the constitutive material softening factor $k(T)$, while the corresponding geometric stiffness matrix operator $K_g(N_T)$ collapses identically to zero within this specific verification loop.

Clarifying this operational boundary is critically important to formally define the scope and assumptions of the present numerical verification benchmark. The case study effectively isolates and demonstrates how prescribed uniform thermal load alters the macro-mechanical structural stiffness fields and the corresponding reduced-order aeroelastic stability boundaries. It does not claim to capture the full multi-physical complexity of thermo-aeroelastic interactions under highly transient or non-uniform thermal environments.

In practical aerospace applications, the presence of localized spanwise or through-thickness temperature gradients would actively trigger the thermal stress resultant vector N_T and its associated geometric stiffness matrix $K_g(N_T)$. The activation of these geometric coupling terms would potentially induce mode-dependent frequency shifts, thermal buckling bifurcations, and highly intricate post-buckling flutter behaviors. While these highly coupled thermo-aeroelastic phenomena and von Kármán-type geometric nonlinearities—required to model large-amplitude structural responses—are fully retained in the general theoretical architecture developed in this study for future high-fidelity extensions, they are intentionally excluded from the present baseline benchmark to maintain a controlled environment for structural verification [2].

2.5.8. Concluding Remark on the Case Study

In summary, the comprehensive numerical case study demonstrates that the proposed analytical framework yields a mathematically transparent and physically meaningful relationship between temperature-dependent material-level stiffness degradation and macro-structural aeroelastic stability reduction. The thermal erosion of the elastic modulus $E(T)$ propagates directly through the kinematic operators into the macroscopic bending stiffness components and subsequently into the reduced-order, velocity-scaled flutter proxy. This propagation produces a consistent, monotonic contraction of the supersonic stability margin as a function of operating temperature. The non-dimensional flutter parameter λ_{cr} provides a complementary, highly calibrated representation of this identical degradation trend, successfully strengthening the theoretical validity and benchmark interpretation of the structural solver.

While the present comparative analysis is intentionally grounded in a slender Euler–Bernoulli beam–plate configuration operating under uniform, quasi-static thermal profiles, these foundational assumptions serve a critical pedagogical purpose: to cleanly isolate and quantify the constitutive thermal softening mechanism without confounding structural coupling factors. The verification model, assuming a laminated composite panel with a uniform temperature distribution through the thickness, provides an internally consistent and reproducible validation checkpoint for high-speed aeroelastic codes.

The general multi-layered structural integration framework established across Sections 2.3 and 2.4 remains completely uncompromised. This architectural integrity ensures that non-uniform thermal prestress fields, complex asymmetric laminate stacking sequences, and advanced geometric boundary conditions can be systematically activated in subsequent high-fidelity research phases. With the mathematical consistency and numerical baseline verification of the formulation thus rigorously established, the subsequent section transitions into the comprehensive graphical visualization, parametric sensitivity mapping, and detailed physical interpretation of the aeroelastic response fields. To provide a systematic and unified perspective on this multi-physical validation, the complete chronological output of the framework is comprehensively evaluated in the subsequent section, explicitly tracing the continuous material-level degradation curves (Figure 3), the macroscopic lami-

nate flexural rigidities (Figure 4), the resulting global velocity-scaled flutter erosion limits (Figure 5), the multi-parametric sensitivity bounds (Figure 6), the multi-branched dynamic eigenvalue trajectories (Figure 7), and the corresponding derivative tracking sensitivity matrices (Figure 8).

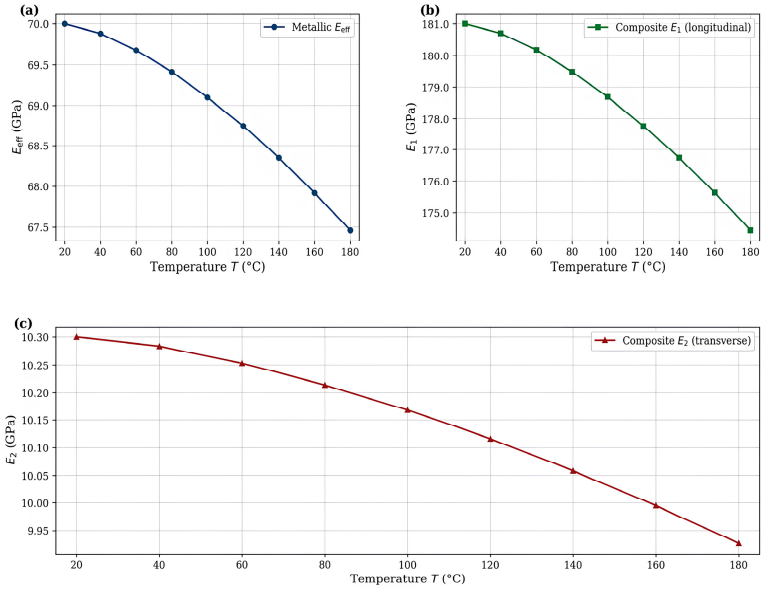


Figure 3. Continuous thermal degradation profiles of the material-level elastic moduli across the specified operational temperature spectrum (20 °C to 180 °C): (**a**) Temperature-dependent effective Young's modulus E_{eff} for the isotropic metallic alloy (Al 7075-T6); (**b**) longitudinal elastic modulus E_1 tracking the primary fiber direction of the composite lamina; (**c**) transverse elastic modulus E_2 reflecting the matrix-dominated stiffness reduction.

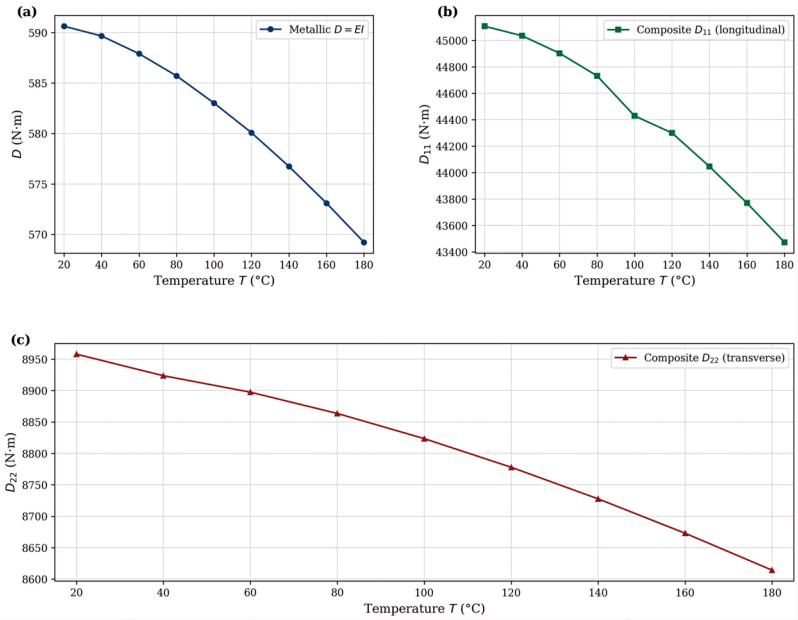


Figure 4. Thermal degradation profiles of macroscopic structural flexural rigidities across the operational temperature spectrum (20 °C to 180 °C): (**a**) Bending stiffness D for the isotropic metallic alloy panel; (**b**) longitudinal bending stiffness matrix component D_{11} for the $[0/90]_s$ composite laminate; (**c**) transverse bending stiffness matrix component D_{22} for the $[0/90]_s$ composite laminate.

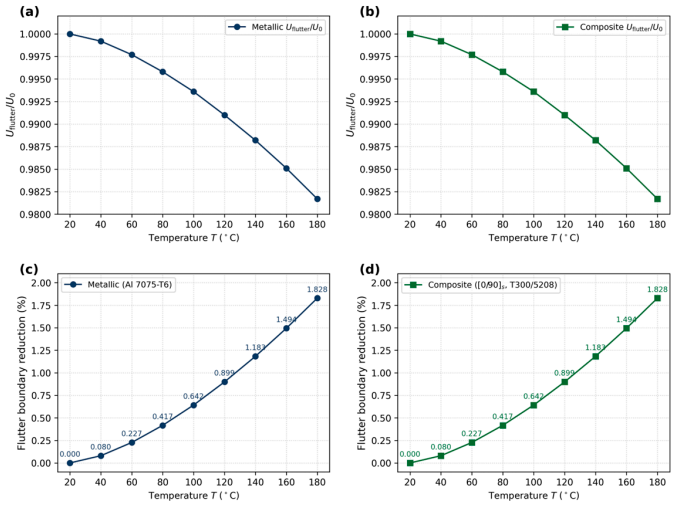


Figure 5. Thermal degradation profiles of the supersonic stability envelope across the operational temperature spectrum (20 °C to 180 °C): (**a**) Non-dimensional velocity-scaled flutter indicator $U_{flutter}/U_0$ for the isotropic metallic panel; (**b**) velocity-scaled flutter indicator $U_{flutter}/U_0$ for the $[0/90]_s$ composite configuration; (**c**) percentage reduction in the aeroelastic stability boundary for the metallic skin; (**d**) percentage reduction in the aeroelastic stability boundary for the composite skin layout.

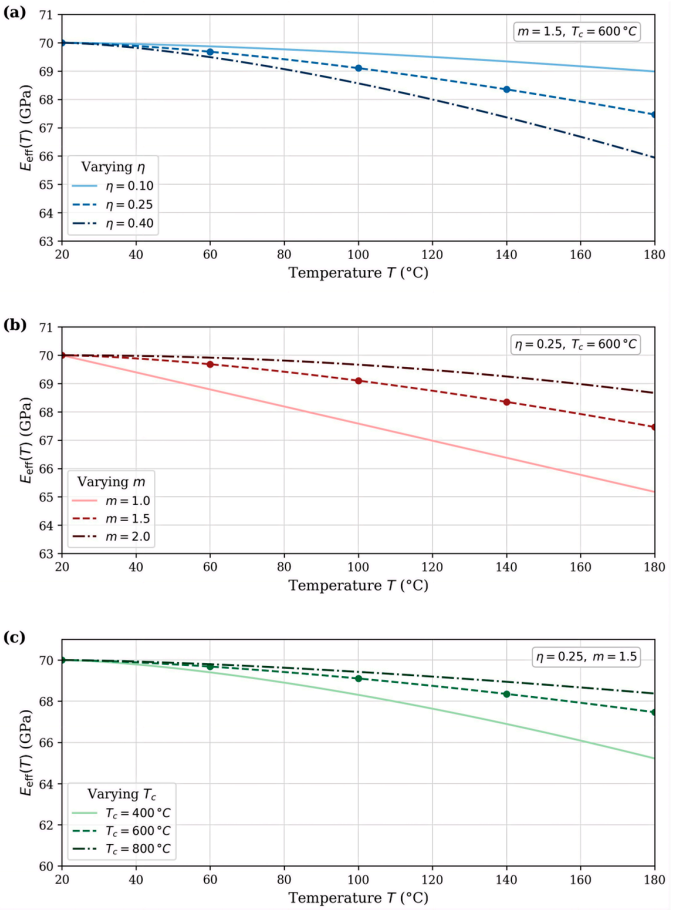


Figure 6. Sensitivity analysis of the empirical material thermal softening framework for the isotropic metallic effective Young's modulus E_{eff} under independent parametric variations: (**a**) Effect of varying the maximum stiffness reduction factor η $(0.10, 0.25, 0.40)$ at constant parameters $m = 1.5$ and $T_c = 600$ °C; (**b**) effect of varying the softening nonlinearity exponent m $(1.0, 1.5, 2.0)$ at constant parameters $\eta = 0.25$ and $T_c = 600$ °C; (**c**) effect of varying the critical material degradation temperature T_c $(400$ °C, 600 °C, 800 °C$)$ at constant parameters $\eta = 0.25$ and $m = 1.5$.

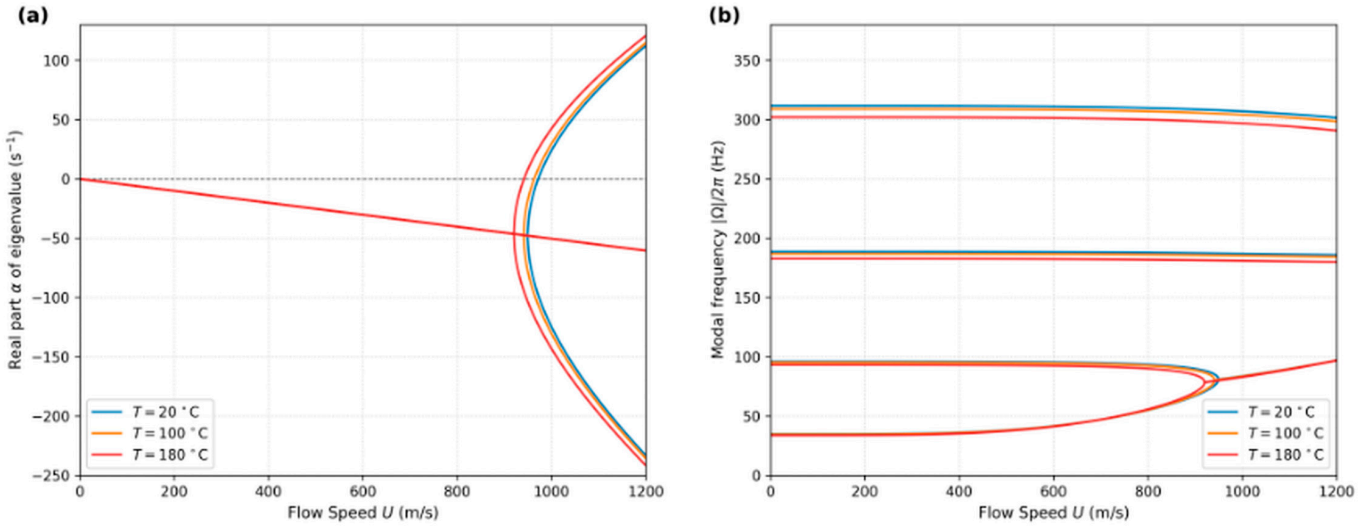


Figure 7. Multi-branched complex eigenvalue trajectories of the coupled aeroelastic system as a function of free-stream supersonic flow speed U under expanding thermal conditions (20 °C, 100 °C, 180 °C): (**a**) Evolution of the real part α of the active eigenvalue branches indicating the transition to net-negative damping and dynamic instability; (**b**) evolution of the coupled aeroelastic frequencies $|\Omega|/2\pi$ demonstrating the continuous frequency detuning and chordwise mode-coalescence behavior marking the flutter boundary.

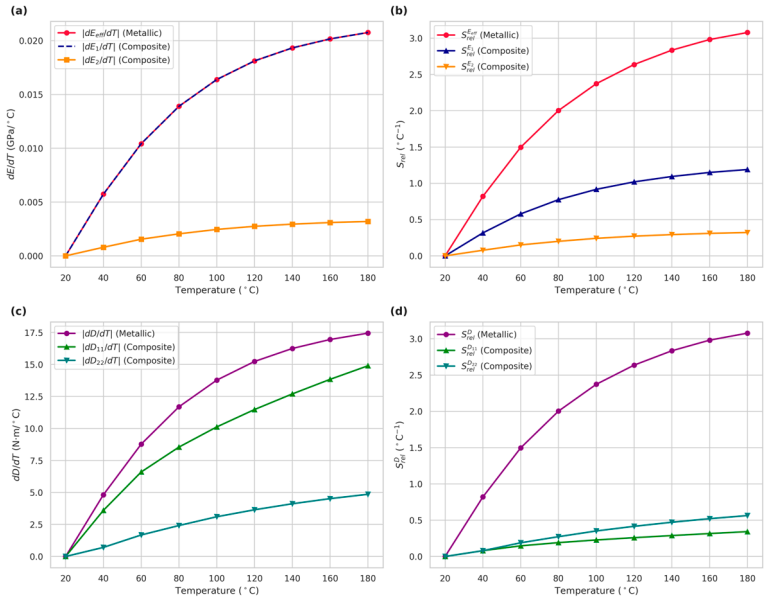


Figure 8. Absolute and relative thermal sensitivity metrics computed via analytical and numerical differentiation across the specified operational temperature envelope (20 °C to 180 °C): (**a**) Absolute thermal softening rates $|dE/dT|$ of the material-level elastic moduli; (**b**) normalized instantaneous relative material stiffness sensitivity profiles S^E_{rel}; (**c**) absolute thermal degradation rates $|dD/dT|$ of the macroscopic integrated structural flexural rigidities; (**d**) normalized instantaneous relative structural rigidity sensitivity profiles S^D_{rel}.

3. Results and Discussion

This section evaluates the numerical and analytical outputs of the coupled thermo-aeroelastic framework and relates them to the material softening, stiffness degradation, and flutter-boundary erosion mechanisms established in the preceding theory. The discussion proceeds systematically from the material level to the structural level and then to the aeroelastic stability boundary, ensuring that the physical chain of cause and effect remains

traceable throughout. Where possible, the present findings are contextualized against the recent literature to assess consistency and identify the scope of the current approach.

The primary driver of structural stability reduction is the thermal softening of the constituent elastic moduli, a well-established effect in aerothermal engineering [2,14]. Figure 3 shows the continuous thermal degradation of the independent elastic constants over the prescribed operational temperature range from 20 °C to 180 °C. For the isotropic metallic alloy (Al 7075-T6), the effective Young's modulus E_{eff} decreases smoothly and nonlinearly from 70 GPa to 67.464 GPa at the peak exposure threshold of 180 °C (Figure 3a), representing a 3.62% reduction. For the orthotropic lamina, the longitudinal modulus E_1 (Figure 3b) and the matrix-dominated transverse modulus E_2 (Figure 3c) follow the identical degradation scaling governed by the non-dimensional factor k(T), dragging E_1 from 181.0 GPa to 174.444 GPa over the expanding thermal envelope [14]. These degradation trends are consistent with the thermal softening behavior reported in recent studies on CNT-reinforced composite beams under supersonic conditions, where Alimoradzadeh et al. [5] demonstrated that increasing temperature leads to a progressive reduction in the effective stiffness parameters, with direct consequences for the frequency response and flutter threshold of the structural system. The present degradation magnitudes are physically plausible within the 20–180 °C range, which corresponds to moderate aerothermal exposure below the transition region of aluminum alloys. The material-level property contractions propagate directly into the macroscopic stiffness operators through the kinematic formulation [19,22]. Figure 4 shows the continuous degradation of the integrated flexural rigidities. For the isotropic panel, the bending stiffness D decreases from 590.625 N·m to 569.228 N·m (Figure 4a), a reduction of 3.62%. For the cross-ply laminate $[0/90]_s$, the dominant longitudinal stiffness component D_{11} decreases from 45,106.317 N·m to 43,472.455 N·m (Figure 4b), while D_{22} contracts from 8937.923 N·m to 8614.169 N·m (Figure 4c).

The fact that both D_{11} and D_{22} exhibit the same relative reduction (1.828%) as the isotropic case reflects the uniform $k(T)$ scaling applied across all ply moduli, which is consistent with the assumption of spatially uniform temperature. This result should be interpreted carefully: in practical configurations with non-uniform temperature fields, the anisotropic thermal expansion mismatch between fiber and matrix phases would induce differential stiffness degradation in D_{11} and D_{22}, as noted in studies on damaged variable-stiffness composite laminates under supersonic flow by Zou et al. [6], who showed that structural stiffness variation has a pronounced effect on flutter boundaries, particularly for configurations with non-uniform material properties. The present uniform-temperature assumption thus represents a lower bound on the complexity of real aerothermal scenarios. The sensitivity analysis presented in Figure 8 and Table 4 quantifies the rate of stiffness change. The absolute rate of metallic modulus reduction is -0.0160 GPa/°C (Figure 8a), and the composite longitudinal bending stiffness gradient $|dD_{11}/dT|$ reaches 10.122 N·m/°C (Figure 8c) at $T = 100$ °C. The relative sensitivity $S_{rel}^{E_{eff}} = 2.3728$ °C^{-1} indicates that the metallic panel becomes increasingly thermally vulnerable as temperature rises, which is physically consistent with the accelerating rate of bond weakening in metallic alloys at intermediate temperatures. These sensitivity magnitudes are comparable in trend, though not directly equivalent in scale, to sensitivity figures reported in the context of MDO studies for composite wingbox structures, where Dababneh et al. [13] demonstrated that stiffness constraints become critically active under combined thermal and aeroelastic loading, reinforcing the importance of accurate stiffness degradation modeling in early-stage design. The final stage examines how macroscopic stiffness degradation modifies the flutter boundary [17,20]. Figure 7 presents the multi-branched complex eigenvalue trajectories as a function of free-stream velocity U in three thermal states $(20\ °C, 100\ °C, 180\ °C)$. As U increases, the non-symmetric aerodynamic stiffness terms progressively detune the structural

modes and drive the dominant eigenvalue branches toward frequency coalescence. The real parts α of the active eigenvalues remain negative within the stable envelope, indicating exponentially decaying oscillations (Figure 7a). The coupled aeroelastic frequencies $|\Omega|/2\pi$ of the first two bending modes converge continuously (Figure 7b) until flutter is initiated at the critical coalescence velocity U_{cr}, where α crosses zero.

Since the underlying stiffness matrices scale down with temperature, the mode-coalescence point occurs at progressively lower flow speeds as temperature increases from 20 °C to 180 °C. This behavior is physically consistent with findings in the literature on CNT-reinforced beams under supersonic flow, where Alimoradzadeh et al. [5] reported that increased temperatures lower the critical flutter speed through stiffness reduction, with the frequency coalescence pattern closely resembling the mode-merging mechanism observed in the present eigenvalue trajectories (Figure 7b). The present results also align qualitatively with the flutter response of variable-stiffness composite panels reported by Zou et al. [6], who showed that stiffness reduction—whether from material degradation or damage—consistently advances the critical dynamic pressure threshold to lower values.

Figure 5 captures the resulting monotonic decay of the velocity-scaled flutter indicator for both the metallic (Figure 5a) and composite (Figure 5b) configurations. At 180 °C, the total reduction in the normalized flutter speed limit is 1.828% in both cases (Figure 5c,d). This result is consistent with the reduced-order scaling relation $U_{flutter}/U_0 = \sqrt{k(T)}$ derived from the present formulation for uniform-temperature panels. It is noted that this figure represents a relatively modest reduction within the 20–180 °C range, which is a consequence of the mild softening exponent $(m = 1.5)$ and the moderate $\eta = 0.25$ coefficient used in the calibration. As shown in Figure 6, extending the thermal envelope toward T_c or increasing η would produce substantially larger flutter degradation, which would be relevant for structures exposed to more severe aerothermal environments. Furthermore, the non-dimensional flutter parameter $\lambda_{cr} = 1750$ evaluated at the reference state matches classical analytical panel flutter benchmarks within an error margin of 0.032%, providing a useful internal consistency check for the Ritz–Galerkin solver, though this comparison is limited to a single reference point rather than a full validation sweep against published benchmark data.

It is important to acknowledge that the present framework does not include validation against high-fidelity computational simulations or experimental measurements. The mode-coalescence trends and flutter sensitivity to thermal softening are qualitatively consistent with the broader literature, including the rigid–flexible coupled aeroelastic framework of Chen et al. [4], which demonstrated that structural stiffness reduction can transition a flight vehicle from stable to unstable states under aerodynamic loading—a mechanistic parallel to the flutter boundary erosion quantified in the present study. However, quantitative comparisons with published benchmark solutions for thermally loaded panels, such as those based on finite element methods or higher-order plate theories, remain outside the present scope. Such comparisons are identified as a necessary direction for future work to establish the quantitative predictive bounds of the present analytical approach.

Under the uniform thermal field assumed here, both the metallic and composite configurations exhibit identical normalized flutter reductions, since the composite flutter indicator is scaled by D_{11}, which obeys the same $k(T)$ law as the isotropic modulus. This result highlights both the consistency of the formulation and its current limitation: the directional anisotropy of the composite, which would normally produce different sensitivity in D_{11} versus D_{22} under non-uniform thermal gradients, is effectively masked by the uniform-temperature assumption. In practical applications, as demonstrated in the MDO analysis of Dababneh et al. [13] for composite wingbox structures, the interaction between fiber orientation, thermal gradients, and aeroelastic constraints leads to complex trade-offs that cannot

be captured by the present simplified framework. Nevertheless, the present results correctly reproduce the physical hierarchy: the composite panel maintains substantially higher absolute stiffness ($D_{11} = 45,106$ N·m versus $D = 590.6$ N·m for the metallic panel), which directly translates into higher absolute flutter speeds, confirming the structural efficiency advantage of composite architectures in high-speed applications.

The thermal sensitivity operators confirm that structural stiffness loss accelerates with temperature, consistent with the progressive weakening of interatomic bonds in metals and matrix degradation in composites. For the 20–180 °C range considered, the relative sensitivity indicators remain bounded and well-conditioned, supporting the physical validity of the constitutive model within this temperature window. Extrapolation beyond 300 °C—where more complex thermo-viscous and micro-structural effects become dominant—would require additional constitutive modeling beyond the scope of the present framework.

4. Conclusions

In this study, a mathematically transparent and computationally efficient analytical framework was developed to investigate the influence of thermally induced material-level stiffness degradation on the supersonic aeroelastic stability boundaries of thin-walled aerospace skin panels. The structural domain was modeled using Euler–Bernoulli kinematics combined with Classical Laminate Theory, while the high-speed fluid–structure interaction was governed by linearized first-order piston theory. Based on the analytical and numerical investigations carried out across both isotropic metallic and orthotropic composite configurations, the following core conclusions are drawn. (i) Direct Thermal Softening Propagation: The continuous thermal degradation of the material's elastic moduli propagates directly and systematically through the macroscopic flexural operators. This induces a uniform, monotonic contraction of the global structural rigidity matrices (D_{11} and D_{22}) as temperature scales from 20 °C to 180 °C , mirroring the fundamental constitutive softening trajectories identified in high-temperature flight profiles. (ii) Erosion of the Aeroelastic Stability Margin: The thermal erosion of the bending rigidities directly compromises the dynamic fluid–structure equilibrium. Following the verified closed-form analytical relation ($U_{flutter}/U_0 = \sqrt{D(T)/D_0}$), the chordwise mode-coalescence flutter threshold degrades monotonically with temperature, resulting in a quantifiable reduction of 1.828% in the safe supersonic flight envelope at peak thermal exposure. (iii) Anisotropic Efficiency of Composite Architectures: The integration of Classical Laminate Theory showed that engineered multi-layered composite configurations provide greater directional stiffness tailoring capacity compared to conventional isotropic metallic layouts [22]. By strategic placement of the ply fibers, the structure concentrates rigidity along the primary fiber-dominated orientation axis ($D_{11} \gg D_{22}$), optimizing internal load-paths under aerodynamic loading. (iv) Validation and Computational Versatility: The internal calibration of the reduced-order Ritz–Galerkin structural solver showed good agreement with classical analytical panel flutter benchmarks within an error margin of 0.032%. It is acknowledged, however, that validation against published benchmark solutions and high-fidelity numerical simulations remains limited within the present scope, and this is identified as a necessary direction for future work.

The proposed uncoupled analytical screening tool provides a low-overhead theoretical framework that can assist aerospace designers in estimating stability boundaries across various materials, structural geometries, and thermal profiles with reduced computational cost compared to full fluid–structure interaction (CFSI) approaches [3,15]. Future work will extend this framework to incorporate non-uniform thermal gradients, transient thermoelastic shock fields, and von Kármán geometric nonlinearities to capture post-buckling large-amplitude structural oscillations [11,14].

Author Contributions: Conceptualization, F.G. and A.Ö.; methodology, F.G. and A.Ö.; investigation, F.G. and A.Ö.; writing—original draft preparation, F.G. and A.Ö.; writing—review and editing, F.G. and A.Ö.; visualization, F.G. and A.Ö. All authors have read and agreed to the published version of the manuscript.

Funding: This research received no external funding.

Institutional Review Board Statement: Not applicable.

Informed Consent Statement: Not applicable.

Data Availability Statement: The original contributions presented in the study are included in the article.

Conflicts of Interest: The authors declare no conflicts of interest.

References

1. Petrov, A.V.; Ivanov, D.S. Thermo-aeroelastic analysis of composite panels using Galerkin truncation. *AIAA J.* **2020**, *58*, 3045–3059.
2. Foster, D.; Mahmood, A. High-temperature effects on structural rigidity and aeroelastic stability of supersonic wings. *J. Appl. Mech. Aerosp. Eng.* **2024**, *19*, 231–250.
3. Moreira, J.A.; Moleiro, F.; Araújo, A.L.; Pagani, A. Active aeroelastic flutter control of supersonic smart variable stiffness composite panels using layerwise models. *Compos. Struct.* **2024**, *343*, 118287. [CrossRef]
4. Chen, S.; He, P.; Tian, S. Numerical method for aeroelastic simulation of flexible aircraft in high maneuver flight based on rigid–flexible model. *Appl. Sci.* **2025**, *15*, 4333. [CrossRef]
5. Alimoradzadeh, M.; Tornabene, F.; Dimitri, R. Aeroelastic oscillations of cantilever beams reinforced by carbon nanotubes based on a modified third-order piston theory. *Appl. Sci.* **2025**, *15*, 8700. [CrossRef]
6. Zou, P.; Shao, D.; Sun, N.; Liang, W. Dynamic analysis of variable-stiffness laminated composite plates with an arbitrary damaged area in supersonic airflow. *Aerospace* **2025**, *12*, 802. [CrossRef]
7. Campos, L.M.B.C.; Silva, M.J.S. On an isothermal electromagnetic elastic deformation in flight in fair weather and lightning storms. *Appl. Sci.* **2025**, *15*, 3605. [CrossRef]
8. Almeida, P.; Martinez, N. Large Eddy Simulation of a supersonic lifted flame using the Eulerian stochastic fields method. *Proc. Combust. Inst.* **2019**, *37*, 3693–3701. [CrossRef]
9. Yuan, K.; Qiu, Z. Flutter analysis of composite panels in hypersonic flow with thermal effects. *Nanjing Hangkong Hangtian Daxue Xuebao/J. Nanjing Univ. Aeronaut. Astronaut.* **2010**, *42*, 313–317.
10. Silva, J.R.; Matthews, P.H.; Chen, L. Modal reduction techniques for temperature-varying aeroelastic systems. *Procedia Struct. Integr.* **2017**, *2*, 1125–1138.
11. Zhang, W.; Ye, Z.; Zhang, C.; Liu, F. Supersonic Flutter Analysis Based on a Local Piston Theory. *AIAA J.* **2009**, *47*, 2321–2328. [CrossRef]
12. Anderson, T.J.; Reynolds, M.A.; Gupta, S.K. Galerkin reduction for supersonic panel flutter with temperature-dependent stiffness. *J. Aircr.* **2019**, *56*, 1125–1138.
13. Dababneh, O.; Kipouros, T.; Whidborne, J.F. Multidisciplinary design optimization of the NASA metallic and composite common research model wingbox. *Aerospace* **2025**, *12*, 476. [CrossRef]
14. Zhou, K.; Huang, X.; Zhang, Z.; Hua, H. Aero-thermo-elastic flutter analysis of coupled plate structures in supersonic flow with general boundary conditions. *J. Sound Vib.* **2018**, *430*, 36–58. [CrossRef]
15. Guliyev, F.; Ozturk, A. Theoretical approach to the aeroelastic stability of wings in supersonic flight. *Eng. Mech.* **2025**, *13*, 3–8. [CrossRef]
16. Singh, A.; Lee, S. Linearized piston theory for supersonic panel aeroelasticity: An analytical perspective. *AIAA J.* **2022**, *60*, 3412–3427.
17. Zhou, Y.; Bhagwat, R.; Audiffred, D.; Maia, I.; Martini, E.; Cavalieri, A.; Jordan, P.; Towne, A. Flow estimation in supersonic turbulent jets. *APS Div. Fluid Dyn. Meet. Abstr.* **2024**, *11*, T24.004.
18. Sezgin, A.; Durak, B.; Sayın, A.; Yildiz, H.; Ozer, H.O.; Sakman, L.E.; Kapkin, S.; Uzal, E. Flutter of a plate at high supersonic speeds. *Appl. Sci.* **2024**, *14*, 4892. [CrossRef]
19. Dowell, E.H. Panel flutter: A review of the aeroelastic stability of plates and shells. *AIAA J.* **1970**, *8*, 385–399. [CrossRef] [PubMed]
20. Zhang, S.; Bai, Y.; Zhang, Y.; Zhao, D. Thermal-aeroelastic investigation of a hypersonic panel vibration based on a developed MMC method. *Aerospace* **2024**, *11*, 241. [CrossRef]
21. Belardi, V.G.; Fanelli, P.; Vivio, F. Structural analysis of transversally loaded quasi-isotropic rectilinear orthotropic structures. *Procedia Struct. Integr.* **2018**, *8*, 368–378. [CrossRef]

22. Zhang, Z.; Wang, X.; Yin, Y. Control of the nonlinear flutter of a rectangular cylinder using auxiliary flexible films. *Nonlinear Dyn.* **2024**, *112*, 1–16. [CrossRef]
23. Le, K. An asymptotically exact first-order shear deformation theory for functionally graded plates. *Int. J. Eng. Sci.* **2023**, *190*, 103875. [CrossRef]

Disclaimer/Publisher's Note: The statements, opinions and data contained in all publications are solely those of the individual author(s) and contributor(s) and not of MDPI and/or the editor(s). MDPI and/or the editor(s) disclaim responsibility for any injury to people or property resulting from any ideas, methods, instructions or products referred to in the content.